



# CHORUS

This is the accepted manuscript made available via CHORUS. The article has been published as:

## Airy-Beam-Enabled Binary Acoustic Metasurfaces for Underwater Ultrasound-Beam Manipulation

Zhongtao Hu, Yaoheng Yang, Lu Xu, Yun Jing, and Hong Chen

Phys. Rev. Applied **18**, 024070 — Published 26 August 2022

DOI: [10.1103/PhysRevApplied.18.024070](https://doi.org/10.1103/PhysRevApplied.18.024070)

1 **Airy Beam-enabled Binary Acoustic Metasurfaces for Underwater Ultrasound Beam Manipulation**

2

3 Zhongtao Hu<sup>1</sup>, Yaoheng Yang<sup>1</sup>, Lu Xu<sup>1</sup>, Yun Jing<sup>2</sup> and Hong Chen<sup>1,3</sup>

4

5 1. Department of Biomedical Engineering, Washington University in St. Louis, Saint Louis, MO 63130, USA

6 2. Graduate Program in Acoustics, The Pennsylvania State University, University Park, Pennsylvania 16802, USA

7 3. Department of Radiation Oncology, Washington University School of Medicine, Saint Louis, MO 63108, USA

8

9

10 \* Address correspondence to Hong Chen, Ph.D. Department of Biomedical Engineering and Radiation Oncology,

11 Washington University in St. Louis. 4511 Forest Park Ave. St. Louis, MO, 63108, USA. Email:

12 hongchen@wustl.edu

13 **Abstract:**

14 Airy beams are peculiar beams that are non-diffracting, self-accelerating, and self-healing, and they have  
15 offered great opportunities for ultrasound beam manipulation. However, one critical barrier that limits the broad  
16 applications of Airy beams in ultrasound is the lack of simply built device to generate Airy beams in water. This work  
17 presents a family of Airy beam-enabled binary acoustic metasurfaces (AB-BAMs) to generate Airy beams for  
18 underwater ultrasound beam manipulation. AB-BAMs are designed and fabricated by 3D printing with two coding  
19 bits: a polylactic acid (which is the commonly used 3D printing material) unit acting as a bit “1” and a water unit  
20 acting as a bit “0”. The distribution of the binary units on the metasurface is determined by the pattern of Airy beam.  
21 To showcase the wavefront engineering capability of the AB-BAMs, several examples of AB-BAMs are designed,  
22 3D printed, and coupled with a planar single-element ultrasound transducer for experimental validation. We  
23 demonstrate the capability of AB-BAMs in flexibly tuning the focal region size and beam focusing in 3D space by  
24 changing the design of the AB-BAMs. The focal depth of AB-BAMs can be continuous and electronical tuned by  
25 adjusting the operating frequency of the planar transducer without replacing the AB-BAMs. The superimposing  
26 method is leveraged to enable the generation of complex acoustic fields, e.g., multi-foci and letter patterns (e.g., “W”  
27 and “U”). The more complex focal patterns are shown to be also continuously steerable by simply adjusting the  
28 operating frequency. Furthermore, the proposed 3D-printed AB-BAMs are simple to design, easy to fabricate, and  
29 low-cost to produce with the capabilities to achieve tunable focal size, flexible 3D beam focusing, arbitrary multipoint  
30 focusing, and continuous steerability, which creates unprecedented potential for ultrasound beam manipulation.

31 **Keywords:** Airy beam, Acoustic metasurface, Ultrasound, Beam focusing, Binary lens.

## 32 I. Introduction

33 The concept of Airy beams originated from quantum mechanics in 1979 [1]. This concept was introduced  
34 into optics in 2007 [2], and was later brought into acoustics in 2014 [3]. As a solution of the Schrödinger equation and  
35 paraxial wave equation, the Airy function gives rise to Airy beams that are non-diffracting, which means that beam  
36 can propagate for a long distance without significantly extending its width. Simultaneously, this beam laterally shifts  
37 in the transverse plane along a parabolic self-accelerating trajectory. When symmetric Airy beams are generated, these  
38 beams can autofocus at a point. Airy beams also exhibit self-healing properties in the sense that the beams reconstitute  
39 themselves and continue their trajectory even after the beam is severely perturbed [4]. Because of these peculiar  
40 properties, Airy beams have attracted extensive attention in the past decade and have been applied in a wide range of  
41 areas, ranging from particle manipulation [5] and trapping [6], laser filamentation [7], light-sheet microscopy [8],  
42 nonlinear optics [9,10], and nondiffracting waveforms generation for electron beams and quantum particles [11,12].

43 Acoustic Airy beams have great potential in acoustic beam manipulation, particle tracking, and acoustic  
44 focusing [13–15]; however, one key challenge that hinders the broad application of acoustic Airy beam is the lack of  
45 simply built device to generate these beams. One approach to generate Airy beams is to use phased arrays, which  
46 generate desired Airy beams by dynamically modulating the phase delay of each independent transducer  
47 element [3,13,16]. Although phased arrays have the advantage of being dynamically programmable, these arrays need  
48 a large number of transducers elements individually addressable by complex electronics [17]. Another promising  
49 approach is to place an acoustic lens in front of a single-element planar transducer. Different design schemes of the  
50 acoustic lens have been proposed, such as tailored acoustic phase mask [18], zero-index medium [19], and  
51 thermoacoustic phase control [20]. However, these acoustic lens are 3D materials that can be bulky or complex in  
52 design.

53 Acoustic metasurfaces, which are 2D materials of subwavelength thickness, offer a great alternative to bulky  
54 3D materials for acoustic wavefront manipulation. Since its inception, the field of acoustic metasurfaces has undergone  
55 rapid expansion [21]. Acoustic metasurfaces enable the design of devices with complex and unprecedented  
56 functionalities and offer opportunities in many applications, such as beam focusing, cloaking, sound absorption, and  
57 anomalous reflection/refraction [22–31]. Among them, beam focusing is one of the most fundamental examples of  
58 wavefront engineering. Acoustic focusing is important not only for fundamental research of wave propagation but  
59 also for applied research in fields such as biomedical imaging, therapy, nondestructive testing, and particle  
60 manipulation [32–34].

61 Several acoustic metasurfaces for generating symmetric Airy beams have been manufactured, including the  
62 space coiling-up structures [35,36], lossy holey structures [37], and Helmholtz-resonator-like structures [38–40].  
63 However, these pioneering studies focused on airborne sound waves with long wavelengths and often require the  
64 manufacturing of subwavelength units with complicated microstructures, which poses challenges to the fabrication  
65 for ultrasound since the typical wavelength is on the millimeter scale. Meanwhile, these structures rely mainly on the  
66 high acoustic impedance mismatch between air and the solid materials used to build these structures. Hence, the lack

67 of sufficient impedance contrast between water and solid materials prevents the use of these designs for underwater  
68 applications [30].

69 The objective of this work is to develop a family of 3D-printable Airy beam-enabled binary acoustic  
70 metasurfaces (AB-BAMs) to enable a broad range of applications in ultrasound wave manipulations. Binary acoustic  
71 metasurfaces have great promise in acoustic wave manipulation by constructing “digital metasurface bits” to acquire  
72 sophisticated functions in wave manipulation [41]. Typically, binary acoustic metasurfaces are designed by  
73 macroscopically arranging two types of subwavelength meta-atoms with “0” and “1” digital states [42]. Recently,  
74 Jiang et al. performed theoretical simulations to show that a binary acoustic metasurface could produce Airy beams in  
75 water [15]. Their numerical simulations showed the capability of the binary phase modulation in generating ultrasharp  
76 focusing Airy beams. In this paper, we propose to develop AB-BAMs by a 3D printing technique using two coding  
77 bits, a polylactic acid unit acting as the bit “1” and a water unit acting as the bit “0. The distribution of the binary unit  
78 on AB-BAMs depends on the pattern of Airy beams. By combining numerical simulations with experimental  
79 measurements, we demonstrate the versatile capability of the 3D-printed AB-BAMs in tuning the focal size, flexible  
80 beam focusing in 3D, and generating a complex beam pattern that are continuously steerable along the axial direction.

## 81 II. Methods

### 82 A. AB-BAM design for single-point focusing

83 In this section, we provide a full description of how the AB-BAM is designed. Considering a circular Airy  
84 beam propagating along the z-axis, the pressure profile of the Airy beam at the initial plane ( $z = 0$ ) can be described  
85 by [43,44]

$$86 \quad p(x, y) = Ai\left(\frac{r_0 - \sqrt{(x-x_0)^2 + (y-y_0)^2}}{\omega}\right) e^{\left(\alpha \frac{r_0 - \sqrt{(x-x_0)^2 + (y-y_0)^2}}{\omega}\right)}, \quad (1)$$

87 where  $Ai(s) = \frac{1}{\pi} \int_0^\infty \cos(t^3/3 + st) dt$  is the airy function,  $r_0$  is a ring parameter related to the radial position of the  
88 primary airy ring and  $\omega$  is the radial scaling factor,  $(x, y)$  represent the coordinates on the initial plane of the  
89 metasurface, and the circle center  $(x_0, y_0)$  decides the center of the initial plane of Airy beam, which directly defines  
90 the focused position of the AB-BAM in the  $xy$ -plane. In addition, the term  $\alpha$  is an exponential decay factor in ensuring  
91 that the wave conveys finite energy, it only affects the amplitude, but does not affect the phase distribution of the Airy  
92 beam ( $\alpha = 0.002$  for all designs in this study henceforth). As an example, the phase extraction in Fig. 1(b) shows the  
93 cross-sections of the Airy beam profiles generated by three different exponential decay factors:  $\alpha_1 = 0.002$ ,  $\alpha_2 =$   
94  $0.05$ , and  $\alpha_3 = 0.1$ . We can see that the decay factor only affects the amplitude of the Airy beam pattern, but not the  
95 phase profile. The set of parameters  $(r_0, \omega)$  are named as property parameters, which determine the focal properties  
96 of the AB-BAM, including the focal depth ( $z_0$ ), full length of half maximum (FLHM) and full width of half maximum  
97 (FWHM).

98 Figure 1(a-d) shows the steps taken to design the AB-BAM for single-point focusing. First, the amplitude  
99  $p(x, y)$  distribution of the Airy beam at its initial plane is calculated. The cross-sectional line of  $p(x, y)$  exhibits an

100 oscillatory and exponential decaying nature with  $p(x, y) = 0$  being the turning point [Fig. 1(a)]. Second, the pressure  
 101 profile is converted to a binary phase with  $\varphi(x, y) = 0$  for  $p(x, y) > 0$  and  $\varphi(x, y) = \pi/2$  for  $p(x, y) < 0$  [Fig. 1(b-  
 102 c)]. Third, the binary phase map is rendered into a 3D-printed model for the design of a circular-shape AB-BAM [Fig.  
 103 1(d)]. Finally, the 3D model is printed using a 3D printer (Ultimaker S5, Ultimaker, Netherlands) using the polylactic  
 104 acid plastic as the filament at a printing resolutions of 0.25 mm and 0.01 mm for the surface and layer, respectively.  
 105 We couple the printed AB-BAM with a planar single-element ultrasound transducer with a center frequency of 500  
 106 kHz and an aperture of 120 mm. in addition, the AB-BAM has a diameter of 120 mm to match the aperture of the  
 107 transducer.

108 The phase delay of each pixel on the metasurface is proportional to its thickness [45]. To produce a phase  
 109 delay of  $\pi/2$ , the thickness of unit '1' ( $d$ ) is calculated using  $\frac{2\pi f}{c_1}d - \frac{2\pi f}{c_2}d = \frac{\pi}{2}$ , where  $c_1$  and  $c_2$  are the sound speed  
 110 of the water and polylactic acid, respectively, and  $f$  is the operating frequency. Thus, the thickness is represented as  
 111  $d = c_1c_2/4f(c_2 - c_1)$ . The pressure transmission coefficient ( $T$ ) of each unit '1' can be calculated using [46]:  $T =$   
 112  $\frac{2Z_r}{2Z_r \cos(2\pi f d/c_2) - i(Z_r^2 + 1)\sin(2\pi f d/c_2)}$ , where the normalized acoustic impedance is given by  $Z_r = Z_2/Z_1$ , the impedance  
 113 of water is given by  $Z_1 = \rho_1c_1$ , and the impedance of polylactic acid is given by  $Z_2 = \rho_2c_2$ . The terms  $\rho_1$  and  $\rho_2$  are  
 114 the densities of water and polylactic acid, respectively.

115 The acoustic properties of polylactic acid material are obtained experimentally using a pulse-echo technique  
 116 in a cubic structure, resulting in a measured sound speed of 2212 m/s, and a density of 1223 kg/m<sup>3</sup>, and absorption of  
 117 3.54 dB/cm for 500 kHz. These measurements matched those reported in previous studies [47,48]. Water as the  
 118 surrounding medium has a sound speed of 1484 m/s and mass density of 998 kg/m<sup>3</sup> at room temperature. The thickness  
 119 of the AB-BAM is calculated to be 2.35 mm for a 500 kHz transducer, which is approximately  $0.8\lambda$  ( $\lambda = 2.97$  mm).  
 120 The metasurface includes two printed parts. The first part is the polylactic acid unit on the metasurface with a depth  
 121 of 2.25 mm that provides  $\pi/2$  phase shift for the 500 kHz transmitted ultrasonic wave. The second portion is the base  
 122 plate printed at a thickness of 0.10 mm, which is needed to stabilize the metasurface. The transmission coefficient is  
 123 99.6% for unit '1', which indicates efficient transmission through the metasurface.

124 The designed AB-BAMs enable flexible and versatile ultrasound beam manipulations. In this study, we  
 125 demonstrate that AB-BAMs can achieve tunable focusing properties, flexible beam focusing, arbitrary multi-point  
 126 focusing, and continuous steering. We can achieve a sharp-focused beam [Fig. 1(e)] with a small FLHM and a large  
 127 FWHM and a needle-focused beam [Fig. 1(f)] with a large FLHM and a small FWHM. The focus of the Airy beams  
 128 can be steered along the center axis of the metasurface. Moreover, the focus can be steered off-axis by moving the  
 129 ring center  $(x_0, y_0)$  from the geometric center  $(0, 0)$  to off-center  $(x_m, y_m) \neq (0, 0)$ . As illustrated in Fig. 1(g), the  
 130 amplitude profile of an Airy beam centered at  $(x_1, y_1)$  is calculated and then transformed into a binary phase profile  
 131 for off-axis steering. The focus of the AB-BAM can also be tuned continuously along propagation direction by  
 132 adjusting the operating frequency of the planar transducer without replacing the AB-BAMs.

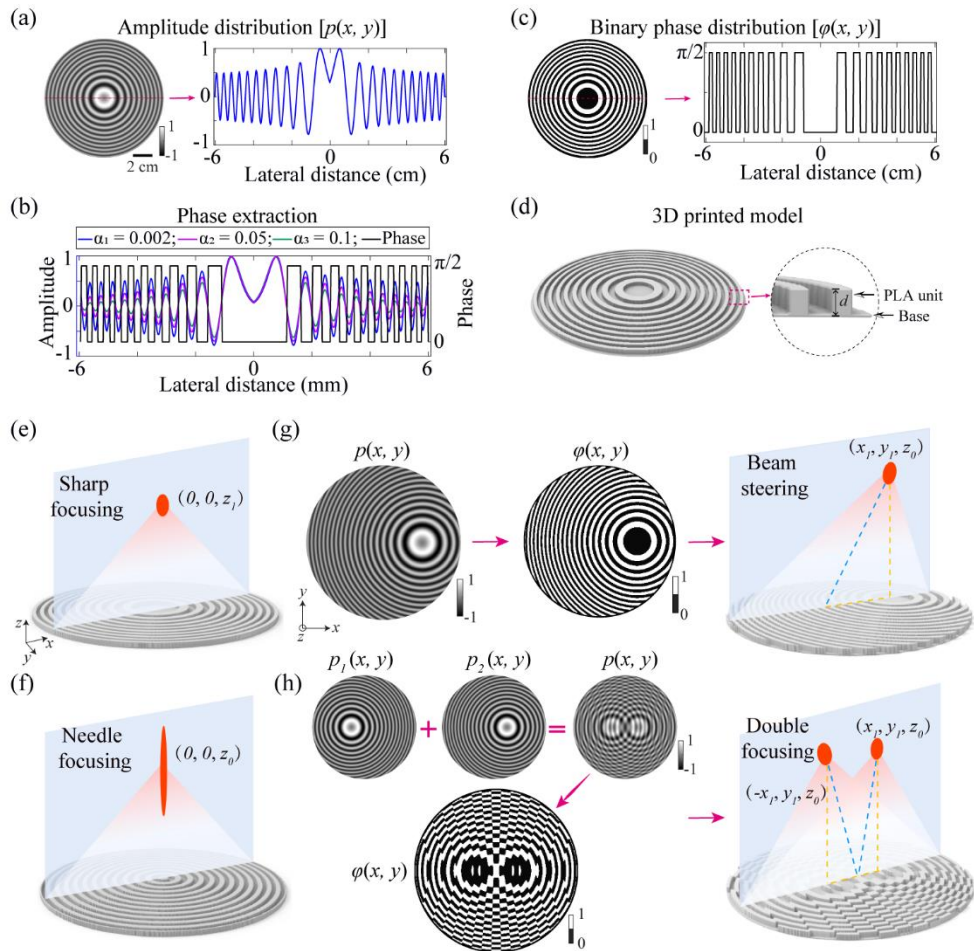
### 133 B. AB-BAM design for multi-point focusing

134 In addition to single-point focusing, AB-BAMs can be designed to generate multifocal points through the  
 135 superimposing method [49]. The final amplitude map  $p(x, y)$  can be expressed as:

$$136 \quad p(x, y) = \sum_m p_m(x, y), m = 1, 2, \dots \quad (2)$$

$$137 \quad p_m(x, y) = Ai\left(\frac{r_0 - \sqrt{(x-x_m)^2 + (y-y_m)^2}}{\omega}\right) e^{\left(\alpha \frac{r_0 - \sqrt{(x-x_m)^2 + (y-y_m)^2}}{\omega}\right)}.$$

138 As a demonstration of this capability, we designed AB-BAMs for double focusing and generating patterns  
 139 of “W” and “U”. For the generation of two foci, the amplitude distribution  $p(x, y)$  at the initial plane is calculated by  
 140 the superposition of the Airy beam patterns with two foci [ $p_1(x, y)$  and  $p_2(x, y)$ ], as illustrated in Fig. 1(h). The  
 141 superimposed amplitude map  $p(x, y)$  is transformed into a binary phase map  $\varphi(x, y)$  to generate an ultrasound field  
 142 with double focusing. The superposition method can be extended to form arbitrary focusing patterns in space, such as  
 143 the letters “W” and “U”.



144  
 145

146 Fig. 1 Design of 3D-printed AB-BAMs. (a) AB-BAM is designed based on the Airy beam amplitude distribution  $p(x, y)$  at the initial plane with  
 147 the beam's cross-sectional line of the amplitude shown on the right side. (b) The term  $\alpha$  is an exponential decay factor that only affects the amplitude,  
 148 but does not affect the phase distribution of the Airy beam. After phase extraction, the pressure distribution is converted into a binary phase profile

149  $\varphi(x, y)$  with the profile's cross-sectional line of the amplitude shown on the right side (c). (d) The black and white circles represent units "1" and  
 150 "0", respectively. The phase profile is then converted to a 3D model of an acoustic metasurface with the metasurface's thickness  $d$  chosen to  
 151 generate a phase delay of  $\pi/2$ . The 3D model is made with a 3D printer using polylactic acid (PLA) filament. The AB-BAM can be designed to tune  
 152 the focusing property. For example, the AB-BAM can generate a focused ultrasound beam with sharp focusing (e) and needle focusing (f). (g)  
 153 Illustration of the AB-BAM designed for off-axis beam focusing. (h) Illustrations of AB-BAM designed for multi-point focusing. Superimposing  
 154 the patterns of Airy beams focused at one point on the left [ $p_1(x, y)$ ] and one point on the right [ $p_2(x, y)$ ] to construct the amplitude distribution of  
 155 double focusing [ $p(x, y)$ ]. The amplitude profile is converted to a binary pattern  $\varphi(x, y)$  and 3D-printed to generate a double-focusing beam.

### 156 C. Numerical simulation and experimental validation

157 Several examples of AB-BAMs are designed and 3D-printed to showcase the wavefront engineering  
 158 capability of the AB-BAMs. We performed numerical simulations and experimental measurements to validate the  
 159 performance of the 3D printed AB-BAMs.

160 Numerical simulations of the 3D acoustic pressure fields generated by the AB-BAMs that are coupled with  
 161 a planar and uniform incident wave is performed using an open-source MATLAB toolbox, k-Wave, and  
 162 pseudospectral method with k-space dispersion correction [50–53]. Cluster computing with one graphics processing  
 163 unit (Nvidia Tesla V100, Nvidia Corporation, Santa Clara, CA, USA) is used to accelerate the 3D simulations. A  
 164 numerical grid with a spatial step of  $\Delta x = \Delta y = \Delta z = 200 \mu\text{m}$  and a numerical temporal step of  $\Delta t = 20 \text{ ns}$  are  
 165 used, which leads to a Courant-Friedrichs-Lewy number of 0.1 and a spatial sampling of approximately 15 grid points  
 166 per wavelength in water for a frequency of 0.5 MHz. These parameters are fixed for all simulations in this study.

167 Experimental validation is carried out by coupling the 3D-printed metasurfaces with the 500 kHz ultrasound  
 168 transducer. The ultrasound transducer is made of a single-element circular lead zirconate titanate (PZT) ceramic (DL-  
 169 20, Del Piezo Specialties LLC, West Palm Beach, FL, USA). Two wires are soldered to the two electrodes of the  
 170 transducer and connected to an electrical driving system composed of a function generator (Model 33500B, Keysight  
 171 Technologies Inc., Englewood, CO, USA) and a power amplifier (1020L, Electronics & Innovation, Rochester, NY,  
 172 USA). The transducer is mounted in a 3D-printed housing. The ultrasound pressure fields are measured using a lipstick  
 173 hydrophone (HGL-200, ONDA Corporation, Sunnyvale, CA) in a water tank filled with degassed and deionized water  
 174 at  $22^\circ$ . The hydrophone is connected to a pre-amplifier (AG-20X0, Onda Corp., Sunnyvale, CA, USA) and a digital  
 175 oscilloscope (Picoscope 5443D, St. Neots, United Kingdom) and is moved in 3D using a computer-controlled 3D  
 176 stage (PK245-01AA, Velmex Inc., NY, USA). The 3D stage is controlled to move at a step size of 0.3 mm over a  
 177 scanning volume that covers the focal patterns of the ultrasound fields. The calibration was conducted by driving the  
 178 ultrasound transducer with a 20-cycle pulsed wave with a pulse repetition frequency of 100 Hz.

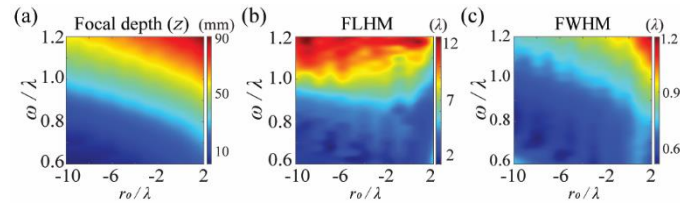
## 179 III Results

### 180 A. Tunable focusing properties

181 The focusing properties of AB-BAMs, which include focal depth, FLHM, and FWHM, are tunable by  
 182 modulating the property parameters ( $r_0, \omega$ ). Over a selected parameter space with  $r_0/\lambda$  in the range of  $[-10, 2]$  and  
 183  $\omega/\lambda$  in the range of  $[0.6, 1.2]$ , numerical simulations show that the focal depth of the ultrasound beam can be tuned



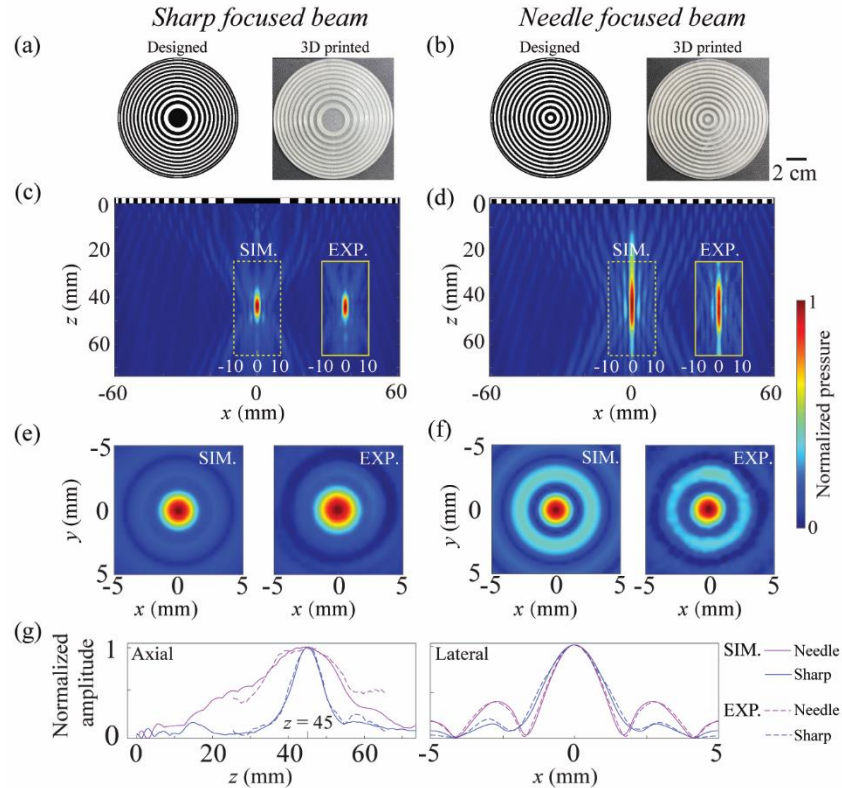
184 from 0.1 mm to 90 mm [Fig. 2(a)], FLHM can vary from  $1.33\lambda$  to  $12.61\lambda$  [Fig. 2(b)], and FWHM can change from  
 185  $0.51\lambda$  to  $1.20\lambda$  [Fig. 2(c)]. The numerical results highlight the flexibility of AB-BAMs in tuning the focusing properties.



186

187 Fig. 2 Tunable focusing properties of AB-BAMs. The operating frequency is 500 kHz,  $r_0/\lambda$  is within the range of  $[-10, 2]$ , and  $\omega/\lambda$  is within the  
 188 range of  $[0.6, 1.2]$ . The simulation results show that (a) the focal depth is tunable from 0.1 mm to 90.0 mm, (b) the FWHM is tunable from  $1.33\lambda$  to  
 189  $12.61\lambda$ , and (c) the FWHM is tunable from  $0.51\lambda$  to  $1.20\lambda$ .

190 Two AB-BAMs are 3D printed to demonstrate the unique capability of AB-BAMs in tuning the focusing  
 191 properties. These two metasurfaces are designed to achieve sharp and needle focusing at the same focal depth  $z =$   
 192  $45$  mm, respectively. Figures 3(a-b) show the designed and 3D-printed AB-BAMs. The sharp focused beam is  
 193 designed with  $(r_0 = 1.73, \omega = 0.89)$ , and the needle-focused beam is designed with  $(r_0 = -9.00, \omega = 1.10)$ . The  
 194 simulated and measured ultrasound fields in the axial plane are presented in Figs. 3(c-d) and the ones for the lateral  
 195 plane are presented in Figs. 3(e-f). The axial and lateral beam profiles across the focal point are shown in Fig. 3(g).  
 196 Numerical simulation finds that the sharp focused beam has a short focal length with an FLHM of  $3.36\lambda$  and FWHM  
 197 of  $0.81\lambda$ . The needle focused beam has an elongated focal region with an FLHM of  $11.15\lambda$  and FWHM of  $0.69\lambda$ . On  
 198 the other hand, the experimental results show that the FLHM and FWHM are  $3.42\lambda$  and  $0.83\lambda$  for the sharp focused  
 199 beam and  $10.96\lambda$  and  $0.72\lambda$  for the needle focused beam. The numerical simulation and experimental measurements  
 200 are in good agreement. These two examples demonstrate that the focusing properties of AB-BAMs are highly tunable  
 201 by modulating the pattern of Airy beams. Different focusing patterns can be used for various ultrasound applications.  
 202 For example, high-intensity focused ultrasound (HIFU) therapy requires a beam with a short axial length to avoid off-  
 203 target effects in the surrounding tissue [54], whereas ultrasound imaging requires a beam with narrow lateral focal  
 204 dimensions to improve the lateral imaging resolution [55].

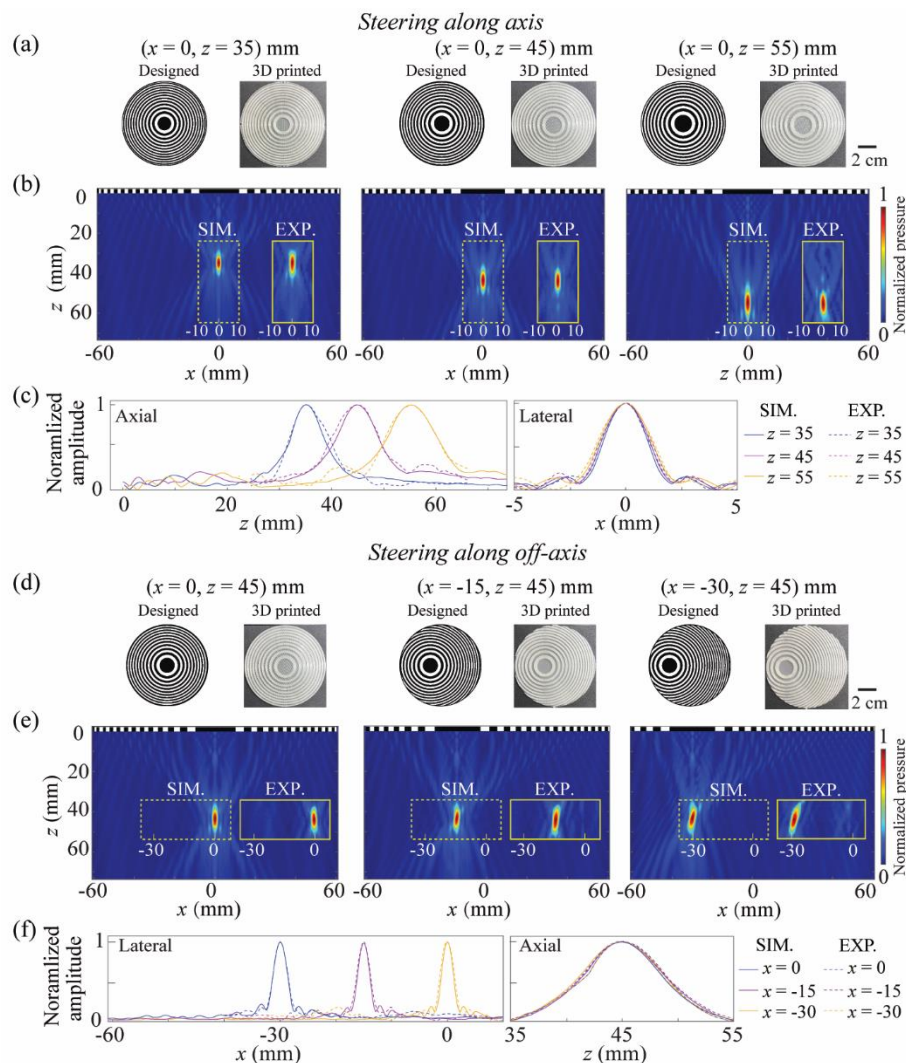


205  
 206 Fig. 3 Two examples to demonstrate the tunable focusing properties of AB-BAMs. AB-BAMs for (a) sharp-focused beam ( $r_0 = 1.73$ ,  $\omega = 0.89$ ),  
 207 and (b) needle-focused beam ( $r_0 = -9.00$ ,  $\omega = 1.10$ ) at a focal depth  $z = 45$  mm are designed (left) and 3D-printed (right). Simulated (SIM.) and  
 208 experimental (EXP.) measured ultrasound pressure fields in the axial  $xz$ -plane are shown for (c) sharp focused beam and (d) needle focused beam.  
 209 The corresponding ultrasound fields in the lateral  $xy$ -plane are presented for the (e) sharp focused beam and (f) needle focused beam. The pressure  
 210 fields are normalized to the peak pressure. (g) Simulated and experimentally measured axial and lateral focal beam profiles across the focal point  
 211 for sharp and needle focused beams. The measured peak pressure of sharp- and needle-focused beams are 0.93 MPa and 0.61 MPa, respectively.

## 212 B. Flexible beam focusing in 3D

213 AB-BAMs have the capability to flexibly adjust their foci in 3D space by changing the design parameters.  
 214 We designed and 3D-printed several AB-BAMs to demonstrate this capability. Figure 4(a) shows the designed and  
 215 3D printed AB-BAMs for beam focusing along the center axis of the metasurface. Three AB-BAMs were designed  
 216 using different sets of property parameters ( $r_0 = 1.38$ ,  $\omega = 0.83$ ), ( $r_0 = 1.73$ ,  $\omega = 0.89$ ), and ( $r_0 = 1.98$ ,  $\omega = 0.97$ )  
 217 to achieve focal depths of  $z = 35$  mm,  $z = 45$  mm, and  $z = 55$  mm, respectively. Figure 4(b) displays the simulated  
 218 and measured ultrasound fields on the  $xz$ -plane. The corresponding normalized axial and lateral focal beam profiles  
 219 for each focal depth are presented in Fig. 4(c). Both the FWHM and FLHM slightly increase as the focal depth  
 220 increases. Based on the simulation results, the FWHMs are  $0.74\lambda$ ,  $0.81\lambda$ , and  $0.88\lambda$ , and the FLHMs are  $2.74\lambda$ ,  $3.36\lambda$ ,  
 221 and  $4.42\lambda$  for the focal depths of  $z = 35$  mm,  $45$  mm, and  $55$  mm, respectively. The corresponding experimental  
 222 results find that the corresponding FWHMs are  $0.79\lambda$ ,  $0.83\lambda$ , and  $0.93\lambda$ , and the FLHMs are  $3.02\lambda$ ,  $3.42\lambda$ , and  $4.45\lambda$ .  
 223 The experimental measurements match the simulation results and agree well with the design.

224 Figure 4(d) shows the designed and 3D printed AB-BAMs for off-axis beam focusing. The circle center  $(x_0,$   
 225  $y_0)$  is set at  $(0, 0)$  mm,  $(-15, 0)$  mm, and  $(-30, 0)$  mm, with a constant focal depth  $z = 45$  mm ( $r_0 = 1.73, \omega =$   
 226  $0.89)$ , to design three AB-BAMs focusing respectively at  $x = 0$  mm,  $x = -15$  mm, and  $x = -30$  mm, respectively.  
 227 Figure 4(e) displays the simulated and measured ultrasound fields on the  $xz$ -plane when the focus is steered off-axis.  
 228 The generated acoustic fields accurately match the simulations. Figure 4(f) presents the corresponding normalized  
 229 axial and lateral beam profiles from the simulations and experiments. As the focused beam steers from 0 mm to -30  
 230 mm off-axis, the FLHM remains almost the same at  $\sim 3.36\lambda$  in simulations and  $\sim 3.42\lambda$  in experiments, while the  
 231 FWHM progressively increases and are from  $0.81\lambda, 0.84\lambda,$  to  $0.97\lambda$  in the simulations and  $0.83\lambda, 0.87\lambda,$  and  $1.02\lambda$  in  
 232 the experiments. The above findings suggest that the focal position of AB-BAMs can be adjusted along the axis and  
 233 off-axis. The 3D arbitrarily focusing property of AB-BAM makes the metasurface a versatile tool for various  
 234 applications.



235

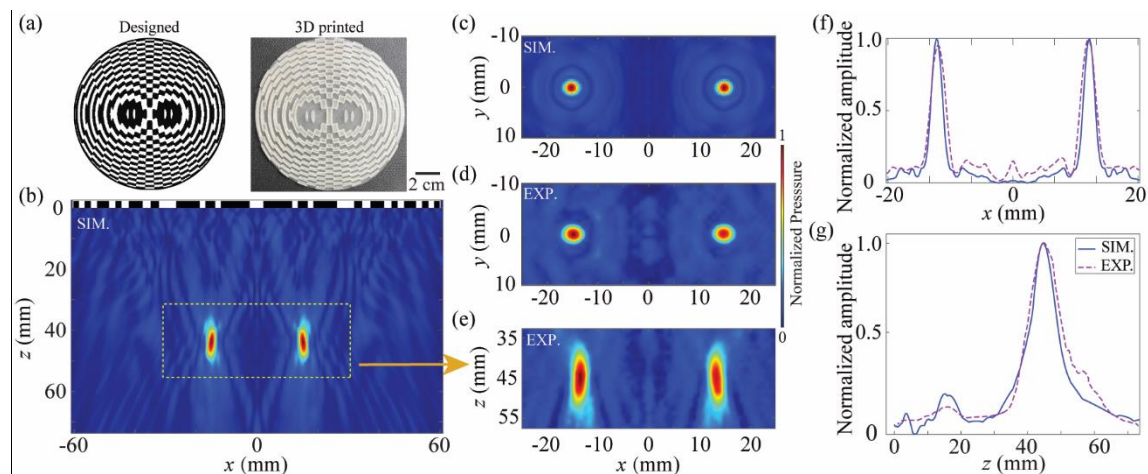
236 Fig. 4. Flexible focusing in 3D space with AB-BAMs. (a) The designed and 3D-printed AB-BAM for steering along the axis at  $x = 0$  with  $z =$   
 237  $35$  mm ( $r_0 = 1.38, \omega = 0.83$ ),  $z = 45$  mm ( $r_0 = 1.73, \omega = 0.89$ ), and  $z = 55$  mm ( $r_0 = 1.98, \omega = 0.97$ ). (b) The simulated and experimentally

238 measured (offset) ultrasound fields in the  $xz$ -plane when steering along the axis with  $z = 35$  mm,  $z = 45$  mm, and  $z = 55$  mm (c) Corresponding  
 239 normalized axial and lateral beam profiles. The measured peak pressures are 0.81, 0.93 and 0.88 MPa for  $z = 35, 45$  and  $55$  mm, respectively. (d)  
 240 The designed and 3D printed AB-BAMs for steering off-axis at  $z = 45$  mm with  $x = 0$  mm,  $x = -15$  mm, and  $x = -30$  mm, respectively. (e)  
 241 Resulting fields from experiments and simulations when steering along off-axis at  $z = 45$  mm with  $x = 0$  mm,  $x = -15$  mm and  $x = -30$  mm.  
 242 (f) Corresponding normalized lateral and axial beam profiles when steering off-axis. The measured peak pressures are 0.93, 0.85 and 0.74 MPa for  
 243  $x = 0, -15$  and  $-30$  mm, respectively.

## 244 C. Arbitrary multi-point focusing

245 The previous results demonstrate the flexibility of AB-BAMs for single-point focusing. In this subsection,  
 246 we extend the applications of AB-BAMs to achieve arbitrary multi-point focusing.

247 Figure 5(a) shows the designed and printed bifocal AB-BAM for the bilateral focus. The focal points were  
 248 set to  $(x = -15, y = 0, z = 45)$ mm and  $(x = 15, y = 0, z = 45)$ mm, respectively, by superimposing the patterns of  
 249 two Airy beams at the initial plane. Specifically, the two Airy beams are designed with the circle center located at  
 250  $(x_0 = -15, y_0 = 0)$ mm and  $(x_0 = 15, y_0 = 0)$ mm using the same property parameters ( $r_0 = 1.73, \omega = 0.89$ ) at a  
 251 focal depth of 45 mm, respectively. Figures 5(b) and 5(e) show the ultrasound fields generated in the  $xz$ -plane by  
 252 simulation and experimental measurements, respectively. The lateral ultrasound fields in the  $xy$ -plane are shown in  
 253 Figures 5(c) and 5(d). Excellent agreement is observed between the simulation and experiments. The lateral and axial  
 254 beamforms across the focus are shown in Figs. 5(f) and 5(g). Additionally, the FWHM and FLHM from the  
 255 experiments ( $0.95\lambda$  and  $3.64\lambda$ , respectively) are in good agreement with the simulations ( $0.87\lambda$  and  $3.53\lambda$ , respectively).

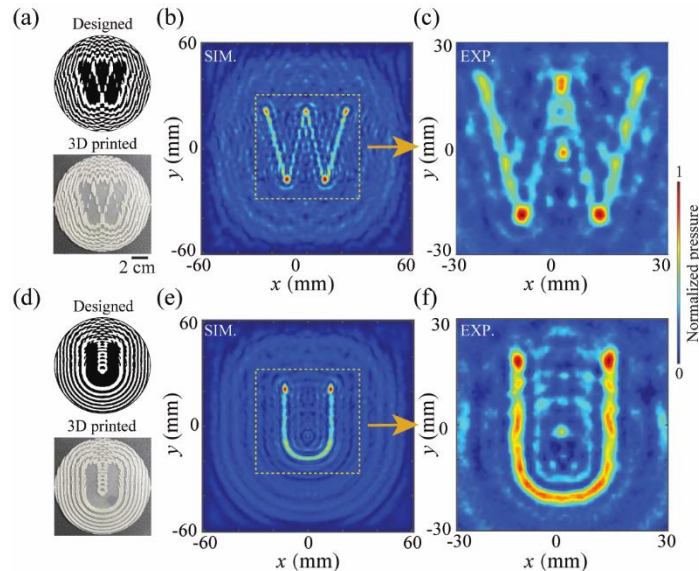


256  
 257 Fig. 5 AB-BAM for double focusing. (a) The designed and 3D-printed AB-BAM for double focusing at  $z = 45$  mm. The ultrasound field in the  
 258  $xz$ -plane by simulation (b) and experiment (e). (c), (d) Corresponding lateral field in  $xz$ -plane. (f), (g) Simulated and experimental;  
 259 measured axial and lateral pressure profiles. The measured peak pressure is 0.73 MPa.

260 Complex multi-point patterns such as the letters “W” and “U” can also be generated by AB-BAMs. Figures  
 261 6(a) and 6(d) show the designed and printed AB-BAMs that generate the letter “W” and “U” patterns in the focal plane  
 262 at  $z = 35$  mm with the property parameters ( $r_0 = 1.38, \omega = 0.83$ ). Figures 6(b) and 6(e) present the simulated  
 263 acoustic pressure fields at the focal plane, where the letters are distinctly visible. Figures 6(c) and 6(f) show the  
 264 experimentally measured ultrasound fields at the focal plane, where both letters are distinctly visible. The simulation



265 and experiment show agreement in the overall shapes of the patterns. The discrepancy between simulation and  
 266 experiment may be attributed to a slight error in the 3D-printed phase profile caused by fabrication error and shear  
 267 mode conversion in the PLA material [56]. These examples demonstrate that arbitrary multi-point focusing can be  
 268 realized by AB-BAMs through the superposition method, which can broaden the applications of acoustic Airy beams.



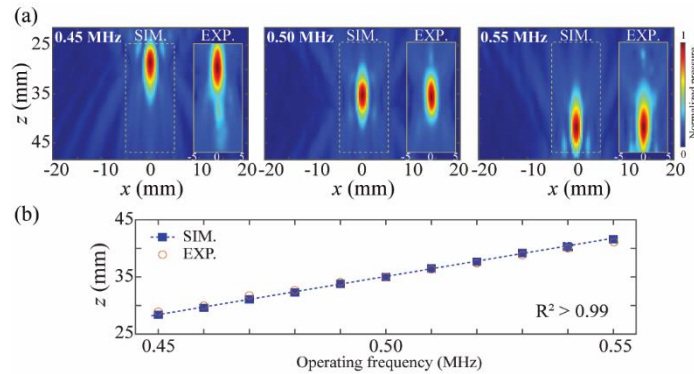
269

270 Fig. 6 Multipoint focusing to generate the letters “W” and “U”. (a) The designed and 3D printed AB-BAM to generate the letter “W”. (b) Simulated  
 271 and (c) experimentally measured pressure fields with the AB-BAM shown in (a). (d) Simulated and 3D-printed AB-BAM to generate the letter “U”.  
 272 (e) Simulated and (f) experimentally measured pressure fields with AB-BAM shown in (d). The focal depth is 35 mm.

## 273 D. Continuously steerable arbitrary pattern focusing

274 One property of the AB-BAM is that it can continuously steer the beam focus along the wave propagation  
 275 direction by modulating the operating frequency of the planar transducer without the need to switch the metasurface.  
 276 In this subsection, we evaluate the continuously steerable properties of the AB-BAM by changing its operating  
 277 frequency for single and multifocal beams.

278 For single-point focusing, we show that designed and 3D-printed AB-BAMs can dynamically tune the focal  
 279 depth from 28.4 mm to 41.6 mm by increasing the operating frequencies from 0.45 to 0.55 MHz. This frequency range  
 280 is within the bandwidth of the planar transducer. A linear relationship ( $R^2 > 0.99$ ) between the focal depth  $z$  and the  
 281 operating frequency is found as shown in Fig. 7(b). The experimental results agreed well with the numerical results,  
 282 with an average relative difference between the experiment and simulation of approximately 3%.

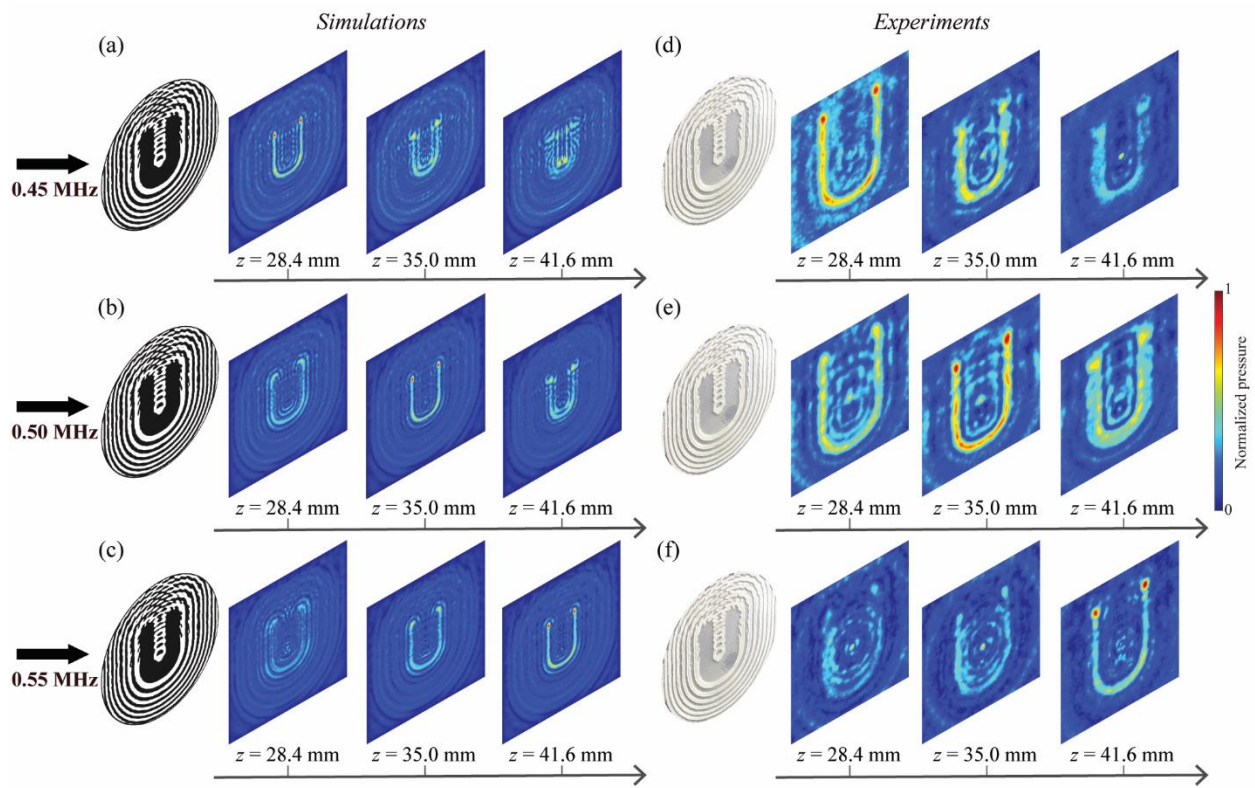


283

284 Fig. 7 Electrical steering of a single focusing point by changing the operating frequency. (a) Simulated and experimentally measured ultrasound  
 285 fields in the  $xz$ -plane at 0.45, 0.50, and 0.55 MHz, respectively. (b) Simulated (solid squares) and experimentally measured (open circles) focal  
 286 depths  $z_0$  from 0.45 to 0.55 MHz. The measured peak pressure varies from 0.82 to 0.98 MPa as the frequency increases from 0.45 to 0.55 MHz.

287 AB-BAMs can also be used to continuously steer an arbitrary focusing pattern, as demonstrated in Fig. 8.  
 288 Figures 8(a) – 8(c) show that the multifocal point beam with the pattern of the letter “U” is steerable to  $z = 28.4$  mm,  
 289  $z = 35.0$  mm, and  $z = 41.6$  mm by changing the operating frequency from 0.45, 0.50 to 0.55 MHz, respectively. As  
 290 shown in Fig. 8(a) – 8(c), the letter “U” is distinctly visible at  $z = 28.4$  mm,  $z = 35.0$  mm, and  $z = 41.6$  mm when  
 291 the frequency increases from 0.45, 0.50, to 0.55 MHz, respectively. Overall, the experimental measurements presented  
 292 in Figs. 8(d) – 8(f) agree well with the simulation results. Thus, the generated multifocal point beam by AB-BAM can  
 293 work over a broad frequency range and be able to continuously steer by the operating frequency.

294

295  
296

297 Fig. 8 Electronical steering of the letter “U” pattern by changing the operating frequency. Simulated pressure field at depths of 28.4 mm, 35.0 mm,  
 298 and 41.6 mm by operating frequency of (a) 0.45 MHz, (b) 0.50 MHz, and (c) 0.55 MHz, respectively. The corresponding experimental pressure  
 299 field under an operating frequency of (d) 0.45 MHz, (e) 0.50 MHz and (f) 0.55 MHz, respectively. Color bar in units normalized to the peak pressure  
 300 of each operating frequency.

#### 301 IV. Conclusion

302 We designed and 3D-printed AB-BAMs for ultrasound beam manipulation and demonstrated their capability  
 303 in ultrasound beam manipulation in water. AB-BAM is a unique binary acoustic lens because it is designed based on  
 304 Airy beams, which have the peculiar properties of non-diffracting, self-accelerating, and self-healing. Several features  
 305 of the AB-BAM are demonstrated. First, AB-BAMs can finely tune the focusing properties such as the FLHM and  
 306 FWHM by changing the property parameters ( $r_0$ ,  $\omega$ ) and customized to various applications. Second, AB-BAMs can  
 307 flexibly adjust the focus in 3D space both along the axis and off-axis by modulating the property parameters ( $r_0$ ,  $\omega$ )  
 308 and circle center ( $x_0$ ,  $y_0$ ). Third, arbitrary multi-point focusing, such as double focusing and even complex pattern  
 309 like letters “W” and “U”, can be achieved through the superimposing method, avoiding the application of iterative  
 310 method during acoustic hologram design, which can effectively reduce the time consumption. Fourth, the focus of the  
 311 AB-BAM can also be tuned continuously by adjusting the operating frequency for both single-point and multi-point  
 312 focusing beam.

313 There are several limitations to this study. First, AB-BAMs are developed for homogeneous media. The  
 314 generated ultrasound beams may be distorted in heterogeneous media such as the skull. The potential solution is to  
 315 design AB-BAMs to couple with ultrasound transducers at lower frequencies such as 200 kHz. At such a low  
 316 frequency, the aberration induced by the skull is not significant. Second, as a proof-of-concept, our experimental  
 317 measurements were conducted with the peak pressures  $< 1$  MPa. Future studies are needed to investigate the generation  
 318 of higher pressure levels for applications such as HIFU therapy. The nonlinear effects associated with high-pressure  
 319 wave propagation will need to be considered when designing the AB-BAM for these applications. Last, the focusing  
 320 properties (FLHM and FWHM) of AB-BAMs are highly related to the acoustic properties of the 3D printing material.  
 321 This study only tested PLA material. Future work is needed to investigate the performance of AB-BAMs printed with  
 322 other materials.

323 It is worth to point out that the printing resolution of the 3D printer determines the upper limit of the operating  
 324 ultrasound frequency of AB-BAMs, and the ultrasound frequency determines the spatial resolution of the resultant  
 325 beam pattern. The practical upper limit of the operating ultrasound frequency depends on the design of each AB-  
 326 BAMs. As an example, the printing resolution ( $R_s$ ) of the 3D printer used in this study was 0.25 mm. The AB-BAM  
 327 designed for beam focusing shown in Fig. 1(g) had a minimal ring spacing ( $D$ ) of 1.25 mm for an operating frequency  
 328 of 0.5 MHz (Freq). Because AB-BAM design parameter was scaled by the wavelength as shown in Fig. 2, the upper  
 329 limit of the operating ultrasound frequency ( $F_{max}$ ) can be calculated as:  $F_{max} = (D \times \text{Freq})/R_s$ . As a result, the  $F_{max}$   
 330 for the AB-BAM shown in Fig. 1(g) is 2.5 MHz.

331 In conclusion, this study demonstrated that 3D-printed AB-BAMs provide a flexible and versatile tool for  
 332 ultrasound beam manipulation. It can be easily and accurately manufactured by 3D printing. Complex acoustic patterns

333 can be generated with the AB-BAMs coupled with a single-element planar ultrasonic transducer. The proposed 3D-  
334 printed AB-BAMs can achieve tunable focal region size, flexible focusing in 3D, arbitrary multipoint focusing, and  
335 continuous steerability, which may have the potential for different applications such as neuromodulation [57], HIFU  
336 therapy [58,59], ultrasound-mediated microbubbles for blood-brain barrier opening for brain drug delivery [60–63] or  
337 enriching the brain tumor-derived molecular biomarkers for sonobiopsy [64–66].

### 338 **Acknowledgment**

339 This work was supported in part by the the National Institutes of Health grants (R01EB027223,  
340 R01EB030102, R01MH116981, and UG3MH126861). It was also partially supported by the Office of Naval Research  
341 (grant number # N00014-19-1-2335).



## 342 Reference

- 343 [1] M. V. Berry and N. L. Balazs, *Nonspreading Wave Packets*, Am. J. Phys. **47**, 264 (1979).
- 344 [2] G. A. Siviloglou, J. Broky, A. Dogariu, and D. N. Christodoulides, *Observation of Accelerating Airy Beams*, Phys. Rev. Lett. **99**,  
345 213901 (2007).
- 346 [3] P. Zhang, T. Li, J. Zhu, X. Zhu, S. Yang, Y. Wang, X. Yin, and X. Zhang, *Generation of Acoustic Self-Bending and Bottle Beams by*  
347 *Phase Engineering*, Nat. Commun. **5**, 4316 (2014).
- 348 [4] N. K. Efremidis, Z. Chen, M. Segev, and D. N. Christodoulides, *Airy Beams and Accelerating Waves: An Overview of Recent*  
349 *Advances*, Optica **6**, 686 (2019).
- 350 [5] J. Baumgartl, M. Mazilu, and K. Dholakia, *Optically Mediated Particle Clearing Using Airy Wavepackets*, Nat. Photonics **2**, 675  
351 (2008).
- 352 [6] P. Zhang, J. Prakash, Z. Zhang, M. S. Mills, N. K. Efremidis, D. N. Christodoulides, and Z. Chen, *Trapping and Guiding*  
353 *Microparticles with Morphing Autofocusing Airy Beams*, Opt. Lett. **36**, 2883 (2011).
- 354 [7] P. Polynkin, M. Kolesik, J. V. Moloney, G. A. Siviloglou, and D. N. Christodoulides, *Curved Plasma Channel Generation Using*  
355 *Ultraintense Airy Beams*, Science (80-. ). **324**, 229 (2009).
- 356 [8] T. Vettenburg, H. I. C. Dalgarno, J. Nylk, C. Coll-Lladó, D. E. K. Ferrier, T. Čížmár, F. J. Gunn-Moore, and K. Dholakia, *Light-Sheet*  
357 *Microscopy Using an Airy Beam*, Nat. Methods **11**, 541 (2014).
- 358 [9] P. Panagiotopoulos, D. G. Papazoglou, A. Couairon, and S. Tzortzakis, *Sharply Autofocused Ring-Airy Beams Transforming into Non-*  
359 *Linear Intense Light Bullets*, Nat. Commun. **4**, 2622 (2013).
- 360 [10] T. Ellenbogen, N. Voloch-Bloch, A. Ganany-Padowicz, and A. Arie, *Nonlinear Generation and Manipulation of Airy Beams*, Nat.  
361 Photonics **3**, 395 (2009).
- 362 [11] I. Kaminer, J. Nemirovsky, M. Rechtsman, R. Bekenstein, and M. Segev, *Self-Accelerating Dirac Particles and Prolonging the*  
363 *Lifetime of Relativistic Fermions*, Nat. Phys. **11**, 261 (2015).
- 364 [12] N. Voloch-Bloch, Y. Lereah, Y. Lilach, A. Gover, and A. Arie, *Generation of Electron Airy Beams*, Nature **494**, 331 (2013).
- 365 [13] S. Zhao, Y. Hu, J. Lu, X. Qiu, J. Cheng, and I. Burnett, *Delivering Sound Energy along an Arbitrary Convex Trajectory*, Sci. Rep. **4**,  
366 6628 (2015).
- 367 [14] F. G. Mitri, *Airy Acoustical-Sheet Spinner Tweezers*, J. Appl. Phys. **120**, 104901 (2016).
- 368 [15] X. Jiang, Y. Li, D. Ta, and W. Wang, *Ultrasonic Sharp Autofocusing with Acoustic Metasurface*, Phys. Rev. B **102**, 064308 (2020).
- 369 [16] K. Mohanty, S. Mahajan, G. Pinton, M. Muller, and Y. Jing, *Observation of Self-Bending and Focused Ultrasound Beams in the*  
370 *Megahertz Range*, IEEE Trans. Ultrason. Ferroelectr. Freq. Control **65**, 1460 (2018).
- 371 [17] K. Melde, A. G. Mark, T. Qiu, and P. Fischer, *Holograms for Acoustics*, Nature **537**, 518 (2016).
- 372 [18] U. Bar-Ziv, A. Postan, and M. Segev, *Observation of Shape-Preserving Accelerating Underwater Acoustic Beams*, Phys. Rev. B **92**,  
373 100301 (2015).
- 374 [19] H. Gao, Z. Gu, B. Liang, X. Zou, J. Yang, J. Yang, and J. Cheng, *Acoustic Focusing by Symmetrical Self-Bending Beams with Phase*  
375 *Modulations*, Appl. Phys. Lett. **108**, 073501 (2016).
- 376 [20] C. Liu, J.-P. Xia, H.-X. Sun, and S.-Q. Yuan, *Thermoacoustic Focusing Lens by Symmetric Airy Beams with Phase Manipulations*, J.  
377 Phys. D: Appl. Phys. **50**, 505101 (2017).
- 378 [21] B. Liang, J. Cheng, and C.-W. Qiu, *Wavefront Manipulation by Acoustic Metasurfaces: From Physics and Applications*, Nanophotonics  
379 **7**, 1191 (2018).
- 380 [22] Y. Li, B. Liang, X. Tao, X. Zhu, X. Zou, and J. Cheng, *Acoustic Focusing by Coiling up Space*, Appl. Phys. Lett. **101**, 233508 (2012).
- 381 [23] G. Ma, M. Yang, S. Xiao, Z. Yang, and P. Sheng, *Acoustic Metasurface with Hybrid Resonances*, Nat. Mater. **13**, 873 (2014).
- 382 [24] Y. Li, X. Jiang, R. Q. Li, B. Liang, X. Y. Zou, L. Yin, and J. C. Cheng, *Experimental Realization of Full Control of Reflected Waves*  
383 *with Subwavelength Acoustic Metasurfaces*, Phys. Rev. Appl. **2**, 064002 (2014).
- 384 [25] S.-D. Zhao, A. L. Chen, Y.-S. Wang, and C. Zhang, *Continuously Tunable Acoustic Metasurface for Transmitted Wavefront*  
385 *Modulation*, Phys. Rev. Appl. **10**, 054066 (2018).
- 386 [26] J. Chen, J. Xiao, D. Lisevych, A. Shakouri, and Z. Fan, *Deep-Subwavelength Control of Acoustic Waves in an Ultra-Compact*  
387 *Metasurface Lens*, Nat. Commun. **9**, 4920 (2018).

- 388 [27] S.-W. Fan, S.-D. Zhao, A.-L. Chen, Y.-F. Wang, B. Assouar, and Y.-S. Wang, *Tunable Broadband Reflective Acoustic Metasurface*, Phys. Rev. Appl. **11**, 044038 (2019).  
389
- 390 [28] S.-W. Fan, S.-D. Zhao, L. Cao, Y. Zhu, A.-L. Chen, Y.-F. Wang, K. Donda, Y.-S. Wang, and B. Assouar, *Reconfigurable Curved Metasurface for Acoustic Cloaking and Illusion*, Phys. Rev. B **101**, 024104 (2020).  
391
- 392 [29] J. He, X. Jiang, H. Zhao, C. Zhang, Y. Zheng, C. Liu, and D. Ta, *Broadband Three-Dimensional Focusing for an Ultrasound Scalpel at Megahertz Frequencies*, Phys. Rev. Appl. **16**, 024006 (2021).  
393
- 394 [30] L. Fan and J. Mei, *Multifunctional Waterborne Acoustic Metagratings: From Extraordinary Transmission to Total and Abnormal Reflection*, Phys. Rev. Appl. **16**, 044029 (2021).  
395
- 396 [31] W. K. Cao, C. Zhang, L. T. Wu, K. Q. Guo, J. C. Ke, T. J. Cui, and Q. Cheng, *Tunable Acoustic Metasurface for Three-Dimensional Wave Manipulations*, Phys. Rev. Appl. **15**, 024026 (2021).  
397
- 398 [32] H. Yang, X. Cao, F. Yang, J. Gao, S. Xu, M. Li, X. Chen, Y. Zhao, Y. Zheng, and S. Li, *A Programmable Metasurface with Dynamic Polarization, Scattering and Focusing Control*, Sci. Rep. **6**, 35692 (2016).  
399
- 400 [33] B. Assouar, B. Liang, Y. Wu, Y. Li, J.-C. Cheng, and Y. Jing, *Acoustic Metasurfaces*, Nat. Rev. Mater. **3**, 460 (2018).
- 401 [34] Z. Hu, Z. An, Y. Kong, G. Lian, and X. Wang, *The Nonlinear S0 Lamb Mode in a Plate with a Linearly-Varying Thickness*, Ultrasonics **94**, 102 (2019).  
402
- 403 [35] D.-C. Chen, X.-F. Zhu, D.-J. Wu, and X.-J. Liu, *Broadband Airy-like Beams by Coded Acoustic Metasurfaces*, Appl. Phys. Lett. **114**, 053504 (2019).  
404
- 405 [36] D.-C. Chen, X.-F. Zhu, Q. Wei, D.-J. Wu, and X.-J. Liu, *Broadband Acoustic Focusing by Airy-like Beams Based on Acoustic Metasurfaces*, J. Appl. Phys. **123**, 044503 (2018).  
406
- 407 [37] Y. Zhu, J. Hu, X. Fan, J. Yang, B. Liang, X. Zhu, and J. Cheng, *Fine Manipulation of Sound via Lossy Metamaterials with Independent and Arbitrary Reflection Amplitude and Phase*, Nat. Commun. **9**, 1632 (2018).  
408
- 409 [38] Y. Zhang, H. Cheng, J. Tian, and S. Chen, *Frequency-Selected Bifunctional Coding Acoustic Metasurfaces*, Phys. Rev. Appl. **14**, 064057 (2020).  
410
- 411 [39] Y. Li, X. Jiang, B. Liang, J. C. Cheng, and L. Zhang, *Metascreen-Based Acoustic Passive Phased Array*, Phys. Rev. Appl. **4**, 024003 (2015).  
412
- 413 [40] J. Qian, B.-Y. Liu, H.-X. Sun, S.-Q. Yuan, and X.-Z. Yu, *Broadband Acoustic Focusing by Symmetric Airy Beams with Phased Arrays Comprised of Different Numbers of Cavity Structures*, Chinese Phys. B **26**, 114304 (2017).  
414
- 415 [41] M. H. Fakhari, H. Rajabalipanah, and A. Abdolali, *Spatiotemporal Binary Acoustic Metasurfaces*, Phys. Rev. Appl. **16**, 024062 (2021).  
416
- 417 [42] B. Xie, K. Tang, H. Cheng, Z. Liu, S. Chen, and J. Tian, *Coding Acoustic Metasurfaces*, Adv. Mater. **29**, 1603507 (2017).  
418
- 419 [43] N. K. Efremidis, D. N. Christodoulides, I. Chremmos, and Z. Chen, *Abruptly Autofocusing Waves*, Opt. InfoBase Conf. Pap. **35**, 4045 (2011).  
420
- 419 [44] D. G. Papazoglou, N. K. Efremidis, D. N. Christodoulides, and S. Tzortzakis, *Observation of Abruptly Autofocusing Waves*, Opt. Lett. **36**, 1842 (2011).  
420
- 421 [45] Z. Lin, X. Guo, J. Tu, Q. Ma, J. Wu, and D. Zhang, *Acoustic Non-Diffracting Airy Beam*, J. Appl. Phys. **117**, 104503 (2015).  
422
- 422 [46] N. Jiménez, V. Romero-García, V. Pagneux, and J.-P. Groby, *Quasiperfect Absorption by Subwavelength Acoustic Panels in Transmission Using Accumulation of Resonances Due to Slow Sound*, Phys. Rev. B **95**, 014205 (2017).  
423
- 424 [47] D. Tarrazó-Serrano, S. Pérez-López, P. Candelas, A. Uris, and C. Rubio, *Acoustic Focusing Enhancement In Fresnel Zone Plate Lenses*, Sci. Rep. **9**, 7067 (2019).  
425
- 426 [48] S. Jiménez-Gambín, N. Jiménez, J. M. Benlloch, and F. Camarena, *Holograms to Focus Arbitrary Ultrasonic Fields through the Skull*, Phys. Rev. Appl. **12**, 014016 (2019).  
427
- 428 [49] F. Lu, L. Tan, Z. Tan, H. Wu, and Y. Liang, *Dynamical Power Flow and Trapping-Force Properties of Two-Dimensional Airy-Beam Superpositions*, Phys. Rev. A **104**, 023526 (2021).  
429
- 430 [50] B. E. Treeby and B. T. Cox, *K-Wave: MATLAB Toolbox for the Simulation and Reconstruction of Photoacoustic Wave Fields*, J. Biomed. Opt. **15**, 021314 (2010).  
431
- 432 [51] T. Y. Park, K. J. Pahk, and H. Kim, *Method to Optimize the Placement of a Single-Element Transducer for Transcranial Focused Ultrasound*, Comput. Methods Programs Biomed. **179**, 104982 (2019).  
433
- 434 [52] N. Wu, G. Shen, X. Qu, H. Wu, S. Qiao, E. Wang, Y. Chen, and H. Wang, *An Efficient and Accurate Parallel Hybrid Acoustic Signal Correction Method for Transcranial Ultrasound*, Phys. Med. Biol. **65**, 215019 (2020).  
435

- 436 [53] Z. Hu, L. Xu, C.-Y. Chien, Y. Yang, Y. Gong, D. Ye, C. P. Pacia, and H. Chen, *3-D Transcranial Microbubble Cavitation Localization*  
437 *by Four Sensors*, IEEE Trans. Ultrason. Ferroelectr. Freq. Control **68**, 3336 (2021).
- 438 [54] S. Kim, Y. Jo, G. Kook, C. Pasquinelli, H. Kim, K. Kim, H. S. Hoe, Y. Choe, H. Rhim, A. Thielscher, J. Kim, and H. J. Lee,  
439 *Transcranial Focused Ultrasound Stimulation with High Spatial Resolution*, Brain Stimul. **14**, 290 (2021).
- 440 [55] Y.-X. Shen, Y.-G. Peng, F. Cai, K. Huang, D.-G. Zhao, C.-W. Qiu, H. Zheng, and X.-F. Zhu, *Ultrasonic Super-Oscillation Wave-*  
441 *Packets with an Acoustic Meta-Lens*, Nat. Commun. **10**, 3411 (2019).
- 442 [56] J. Li, A. Crivoi, X. Peng, L. Shen, Y. Pu, Z. Fan, and S. A. Cummer, *Three Dimensional Acoustic Tweezers with Vortex Streaming*,  
443 Commun. Phys. **4**, 113 (2021).
- 444 [57] W. Legon, L. Ai, P. Bansal, and J. K. Mueller, *Neuromodulation with Single-Element Transcranial Focused Ultrasound in Human*  
445 *Thalamus*, Hum. Brain Mapp. **39**, 1995 (2018).
- 446 [58] T. Li, H. Chen, T. Khokhlova, Y.-N. Wang, W. Kreider, X. He, and J. H. Hwang, *Passive Cavitation Detection during Pulsed HIFU*  
447 *Exposures of Ex Vivo Tissues and In Vivo Mouse Pancreatic Tumors*, Ultrasound Med. Biol. **40**, 1523 (2014).
- 448 [59] Y. Zhang, J.-F. Aubry, J. Zhang, Y. Wang, J. Roy, J. F. Mata, W. Miller, E. Dumont, M. Xie, K. Lee, Z. Zuo, and M. Wintermark,  
449 *Defining the Optimal Age for Focal Lesioning in a Rat Model of Transcranial HIFU*, Ultrasound Med. Biol. **41**, 449 (2015).
- 450 [60] H. Chen and E. E. Konofagou, *The Size of Blood-Brain Barrier Opening Induced by Focused Ultrasound Is Dictated by the Acoustic*  
451 *Pressure*, J. Cereb. Blood Flow Metab. **34**, 1197 (2014).
- 452 [61] N. Lipsman, Y. Meng, A. J. Bethune, Y. Huang, B. Lam, M. Masellis, N. Herrmann, C. Heyn, I. Aubert, A. Boutet, G. S. Smith, K.  
453 Hynynen, and S. E. Black, *Blood-Brain Barrier Opening in Alzheimer's Disease Using MR-Guided Focused Ultrasound*, Nat.  
454 Commun. **9**, 2336 (2018).
- 455 [62] K.-T. Chen, W.-Y. Chai, Y.-J. Lin, C.-J. Lin, P.-Y. Chen, H.-C. Tsai, C.-Y. Huang, J. S. Kuo, H.-L. Liu, and K.-C. Wei,  
456 *Neuronavigation-Guided Focused Ultrasound for Transcranial Blood-Brain Barrier Opening and Immunostimulation in Brain Tumors*,  
457 Sci. Adv. **7**, (2021).
- 458 [63] Z. Hu, S. Chen, Y. Yang, Y. Gong, and H. Chen, *An Affordable and Easy-to-Use Focused Ultrasound Device for Noninvasive and*  
459 *High Precision Drug Delivery to the Mouse Brain*, IEEE Trans. Biomed. Eng. **9294**, 1 (2022).
- 460 [64] L. Zhu, G. Cheng, D. Ye, A. Nazeri, Y. Yue, W. Liu, X. Wang, G. P. Dunn, A. A. Petti, E. C. Leuthardt, and H. Chen, *Focused*  
461 *Ultrasound-Enabled Brain Tumor Liquid Biopsy*, Sci. Rep. **8**, 6553 (2018).
- 462 [65] Y. Meng, C. B. Pople, S. Suppiah, M. Llinas, Y. Huang, A. Sahgal, J. Perry, J. Keith, B. Davidson, C. Hamani, Y. Amemiya, A. Seth,  
463 H. Leong, C. C. Heyn, I. Aubert, K. Hynynen, and N. Lipsman, *MR-Guided Focused Ultrasound Liquid Biopsy Enriches Circulating*  
464 *Biomarkers in Patients with Brain Tumors*, Neuro. Oncol. **23**, 1789 (2021).
- 465 [66] C. P. Pacia, J. Yuan, Y. Yue, L. Xu, A. Nazeri, R. Desai, H. M. Gach, X. Wang, M. R. Talcott, A. A. Chaudhuri, G. P. Dunn, E. C.  
466 Leuthardt, and H. Chen, *Sonobiopsy for Minimally Invasive, Spatiotemporally-Controlled, and Sensitive Detection of Glioblastoma-*  
467 *Derived Circulating Tumor DNA*, Theranostics **27**, 362 (2022).
- 468